

Effects of Non-uniform Heat Generation on Magnetized Casson-Williamson Nanofluid Flow Towards a Dissipative Stagnation Point

Mathias John Fuseini¹ and Christian John Etwire^{1,*}

¹Department of Mathematics, School of Mathematical Sciences, C. K. Tedam University of Technology and Applied Sciences, P.O. Box 24, Navrongo, Ghana.

Received: 1 Nov. 2024, Revised: 20 Nov. 2024, Accepted: 15 Dec. 2024

Published online: 1 Jan. 2025

Abstract: In this study, we investigate the impact of non-uniform heat generation on the flow of magnetized Casson-Williamson nanofluid towards a dissipative stagnation point. The research framework incorporates chemical reaction and convective heat transfer into a mathematical model and transformed the governing partial differential equations into nonlinear ordinary differential equations through similarity variables. These equations were solved using fourth-order Range-Kutta method in conjunction with the Newton-Raphson shooting technique. The results for the Nusselt number of the current model were juxtaposed with available work in literature and excellent agreement had been established. The results revealed that the magnetic field parameter significantly influenced the velocity, temperature, and concentration profiles, with Casson nanofluid showing enhanced thermal properties while Williamson nanofluid excelling in mass transfer efficiency. This indicates that Casson nanofluid is a superior fluid for enhancing thermal systems like heat exchangers, While Williamson nanofluid is suitable for processes requiring efficient mass transfer, such as industrial mixing. These insights contribute to the design of advanced biomedical, energy management and cooling devices.

Keywords: Dissipative, Generation, Magnetized, Non-uniform, Stagnation,

1 Introduction

The study of fluid dynamics involving non-Newtonian fluids have gained significant attention in recent years, particularly in the context of industrial and engineering applications. Among these fluids, Casson and Williamson exhibit unique rheological properties which allow them to be used in complex systems. Casson-Williamson fluids, as non-Newtonian fluids, are critical in diverse fields due to their variable viscosity and yield stress properties. In biomedicine, they model blood flow and assist in drug delivery. The food and cosmetics industries use them for products that require precise texture and spreadability. In petroleum and chemical engineering, they aid in drilling and polymer processing. These fluids also optimize applications in coating, printing, lubrication and wastewater treatment through adaptable flow characteristics. [1] examined free convection on a vertical stretching surface with suction and blowing and found surface mass transfer to influence the heat transfer

mechanism. [2] reported on mixed convection boundary layer flow of viscous fluid towards a stagnation point on a vertical stretching surface and noted dual solution to exist within a specific range of the buoyancy parameter for opposing flow, whereas for assisting flow, a unique solution was found. [3] employed homotopy analysis method to obtain an analytical solution for stagnation point flow of viscous fluids towards a stretching sheet. [4] examined the impact of suction/blowing and thermal radiation on steady boundary layer stagnation point flow and heat transfer over a porous shrinking sheet and found the velocity ratio parameter to increase suction but decreased the blowing effect. [5] investigated Casson fluid flow and heat transfer over nonlinear stretching surface and observed the Casson parameter to suppress the velocity field. [6] examined MHD boundary layer flow and heat transfer of nanofluids over a nonlinear stretching sheet. It was established that the temperature of the fluid increased with magnetic parameter, and the thermal boundary layer thickness also increased with

* Corresponding author e-mail: cetwire@cktutas.edu.gh

Brownian motion and thermophoresis parameters. [7] examined Casson fluid flow over a porous exponential stretching surface with radiation and established that highly permeable surfaces cool more rapidly than less porous ones. [8] explored magnetohydrodynamic boundary layer flow of Non-Newtonian Casson fluid over a magnetized exponential stretching surface. It was found that the induced magnetization of the sheet increased the thickness of the thermal boundary layer, leading to significant reduction in heat transfer. [9] investigated the effects of Chemical reaction and thermal radiation on magnetohydrodynamics flow of Casson-Williamson nanofluid over a porous stretching surface and observed the Williamson Parameter to reduce the velocity of the nanofluid. [10] examined heat and mass transfer characteristics of a non-Newtonian Williamson nanofluid flow and revealed that properties of Williamson nanofluid such as viscosity and thermal conductivity impacted heat and mass transfer processes. [11] examined MHD flow of Casson and Williamson fluids under the effects of nonlinear radiation, Viscous dissipation, thermo diffusion and Dufour effects. The results indicated that Casson parameter enhanced the skin friction coefficient and heat and mass transfer. [12] analyzed energy and mass transfer in the flow of Casson hybrid nanofluid over an exponential stretching sheet. It was found that the suction parameter and Darcy-Forchheimer effects significantly decreased the energy transfer rate of hybrid nanofluid. [13] employed Cattaneo-Christov theory to analyse Soret-Dufour effects on MHD Casson nanofluid dynamics over a stretching sheet. [14] examined magnetohydrodynamic flow of Casson nanofluid over an exponential stretching surface with chemical reaction and thermal radiation. The Sherwood number was noted to appreciate with the thermal radiation parameter. [15] thermally analysed ferro Casson nanofluid flow over a Riga plate with thermal radiation and non-uniform heat source/sink and observed enhancement in the thermal boundary layer thickness with radiation. [16] studied the effects of radiative heat and mass on Casson and Williamson nanofluid flow over a porous stretching sheet with chemical reaction and magnetic field. The magnetic field and Brownian motion parameters were noticed to elevate the temperature of the fluid. [17] numerically explored chemically dissipative MHD mixed convective non-Newtonian nanofluid stagnation point flow over an inclined stretching sheet with thermal radiation. The study found the skin friction coefficient to increase significantly with tilt angles and thermophoretic parameter. The existing literature provides limited insight into the complex flow behaviour of Casson-Williamson nanofluid under diverse transport dynamics. Thus, this study sought to explore the effects of non-uniform heat generation on the boundary layer flow of magnetized Casson-Williamson nanofluid towards a dissipative stagnation point. This research has direct implications for industrial processes such as the design of heat exchangers, cooling systems and energy storage devices.

2 Mathematical Model

Consider a steady, laminar, incompressible, two-dimensional flow of viscous and electrically conductive Casson-Williamson nanofluid over a linear stretching surface directed towards a magnetized stagnation point as illustrated in figure (1). The flow is constrained within the xy -plane, with the x -axis aligned along the stretching surface and the y -axis oriented normal to it. The velocity of the stretching sheet is defined as $u_w = ax$, while the free-stream velocity is represented by $u_e = bx$, where $a, b > 0$ are positive constants. The externally imposed transverse magnetic field is assumed to be perpendicular to the stretching surface. The induction effects attributed to external magnetic and electric fields are considered to be negligible. In accordance with boundary layer approximation, alongside the assumptions made, and recognizing that $\tau_{ij} = \mu \left(\left(1 + \frac{1}{\beta}\right) \frac{\partial u}{\partial y} + \frac{\Gamma}{\sqrt{2}} \left(\frac{\partial u}{\partial y}\right)^2 \right)$ [9] serves as the shear stress of the Casson-Williamson nanofluid, the governing equations of continuity, momentum, energy and concentration that encapsulate the flow problem can be articulated as follows:

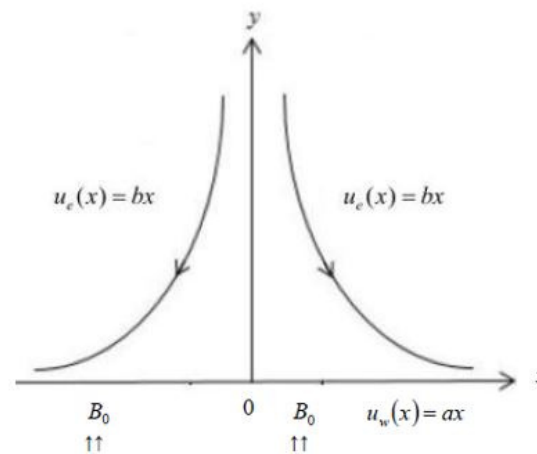


Fig. 1: Schematic diagram of the flow problem.

$$\frac{\partial u}{\partial x} + \frac{\partial v}{\partial y} = 0, \quad (1)$$

$$\begin{aligned} u \frac{\partial u}{\partial x} + v \frac{\partial u}{\partial y} = & v \left(1 + \frac{1}{\beta} \right) \frac{\partial^2 u}{\partial y^2} + u_e \frac{\partial u_e}{\partial x} \\ & + \sqrt{2} v \Gamma \frac{\partial u}{\partial y} \frac{\partial^2 u}{\partial y^2} + \frac{v}{k'} (u_e - u) \\ & + \frac{\sigma B_0^2}{\rho} (u_e - u), \end{aligned} \quad (2)$$

$$u \frac{\partial T}{\partial x} + v \frac{\partial T}{\partial y} = \alpha \frac{\partial^2 T}{\partial y^2} + \frac{\mu}{\rho c_p} \left[\left(1 + \frac{1}{\beta}\right) \left(\frac{\partial u}{\partial y}\right)^2 + \frac{\Gamma}{\sqrt{2}} \left(\frac{\partial u}{\partial y}\right)^3 \right] + \tau \left(D_B \frac{\partial C}{\partial y} \frac{\partial T}{\partial y} + \frac{D_T}{T_\infty} \left(\frac{\partial T}{\partial y}\right)^2 \right) + \frac{Q}{\rho c_p} \tag{3}$$

$$u \frac{\partial C}{\partial x} + v \frac{\partial C}{\partial y} = D_B \frac{\partial^2 C}{\partial y^2} - \gamma(C - C_\infty) + \frac{D_T \partial^2 T}{T_\infty \partial y^2} \tag{4}$$

where u and v represent the x and y components of the velocity respectively, ρ denotes the density of the nanofluid, while μ and ν signify the dynamic and kinematic viscosities of the nanofluid respectively, κ' indicates the permeability of the porous medium, D_B represents the Brownian diffusion coefficient, D_T represents the thermophoresis diffusion, τ denotes the ratio of the effective heat capacity of the nanoparticle material to that of the fluid, T represents the temperature of the nanofluid, C represents the concentration of the nanofluid, c_p refers to the specific heat constant, γ denotes the reaction rate, β signifies the Casson parameter, Γ represents the Williamson parameter, B_o depicts the uniform magnetic field, u_e denotes the free stream velocity and Q signifies non-uniform heat generation as defined by [6]

$$Q = \frac{\alpha u_w}{x\nu} [A^*(T_w - T_\infty)f'(\eta) + B^*(T - T_\infty)] \tag{5}$$

At the surface of the plate when $y = 0$, the boundary conditions are:

$$u(x, 0) = \left(a + \frac{\sigma B_o^2}{\rho}\right)x, \quad v(x, 0) = 0, \tag{6}$$

$$T(x, 0) = T_w, \quad C(x, 0) = C_w.$$

At far away from the surface when $y \rightarrow \infty$, the boundary conditions are:

$$u(x, \infty) \rightarrow u_e(x, \infty) = bx, T(x, \infty) \rightarrow T_\infty, C(x, \infty) \rightarrow C_\infty. \tag{7}$$

2.1 Similarity Transformation

A similarity solution for equations (1) – (2) and (3) – (4) is derived by introducing the independent dimensionless variable η , the dependent variable $f(\eta)$, the dimensionless temperature $\theta(\eta)$ and the dimensionless concentration $\phi(\eta)$, expressed as:

$$\eta = y \sqrt{\frac{a}{\nu}}, \quad u = axf'(\eta), \quad u_e = bx, \quad v = -\sqrt{a\nu}f(\eta),$$

$$\theta(\eta) = \frac{T - T_\infty}{T_w - T_\infty}, \quad \phi(\eta) = \frac{C - C_\infty}{C_w - C_\infty}. \tag{8}$$

By substituting the relevant terms into equations (1) – (4), the resulting coupled nonlinear differential equations are obtained as:

$$\left(1 + \frac{1}{\beta}\right) f'''(\eta) + f(\eta)f''(\eta) - (f'(\eta))^2 + We f''(\eta)f'''(\eta) + (M + \kappa)(\lambda - f'(\eta)) + \lambda^2 = 0. \tag{9}$$

$$\theta''(\eta) + Prf(\eta)\theta'(\eta) + B_r \left(\left(1 + \frac{1}{\beta}\right) f''^2(\eta) + \frac{We}{2} f''^3(\eta) \right) + Pr(N_b \phi'(\eta)\theta'(\eta) + N_t \theta^2(\eta)) + A^* f'(\eta) + B^* \theta(\eta) = 0 \tag{10}$$

$$\phi''(\eta) + Scf(\eta)\phi'(\eta) - Sc\omega\phi(\eta) + \frac{N_t}{N_b} \theta''(\eta) = 0 \tag{11}$$

subject to the boundary conditions:

$$f'(0) = 1 + M, \quad f(0) = 0, \quad \theta(0) = 1, \quad \phi(0) = 1 \quad \text{at} \quad \eta = 0 \tag{12}$$

$$f(\infty) \rightarrow 0, \quad \theta(\infty) \rightarrow 0, \quad \phi(\infty) \rightarrow 0 \quad \text{as} \quad \eta \rightarrow \infty. \tag{13}$$

Here, the prime denotes differentiation with respect to η , while the parameters are defined as follows: λ represents the velocity parameter, k denotes the permeability parameter, We is the Weissenberg number M stands for the magnetic field parameter, Sc represents the Schmidt number, ω is the chemical reaction parameter, N_b is the Brownian motion parameter, N_t is the thermophoresis parameter B_r corresponds to the Brinkman number and Pr is the Prandtl number. The embedded parameters are expressed as:

$$\lambda = \frac{b}{a}, \quad \kappa = \frac{\nu}{\alpha \kappa'}, \quad We = \sqrt{x} \sqrt{\frac{2a^3}{\nu}}, \quad M = \frac{\sigma B_o^2}{\rho a},$$

$$Sc = \frac{\nu}{D_B}, \quad \omega = \frac{\gamma}{a}(C_w - C_\infty), \quad N_b = \frac{\tau D_B (C_w - C_\infty)}{\nu},$$

$$N_t = \frac{\tau D_T (T_w - T_\infty)}{\nu T_\infty}, \quad B_r = \frac{\mu a^2 x^2}{\kappa (T_w - T_\infty)}, \quad Pr = \frac{\nu}{\alpha}.$$

The local skin friction coefficient (C_f), Nusselt number (Nu) and Sherwood number (Sh), which are of practical interest to engineers are respectively defined as:

$$C_f = \frac{\tau_w}{\rho u_w^2}, Nu = \frac{Xq_w}{\kappa(T_w - T_\infty)}, Sh = \frac{Xq_m}{D_B(C_w - C_\infty)} \tag{14}$$

Here, τ_w represents the wall shear stress, q_w denotes the wall heat flux and q_m is the wall mass flux which are respectively defined as:

$$\tau_w = \mu \left[\left(1 + \frac{1}{\beta}\right) \frac{\partial u}{\partial y} + \frac{\Gamma}{\sqrt{2}} \left(\frac{\partial u}{\partial y}\right)^2 \right]_{y=0},$$

$$q_w = -\kappa \frac{\partial T}{\partial y} \Big|_{y=0}, \tag{15}$$

$$q_m = -D_B \frac{\partial C}{\partial y} \Big|_{y=0}.$$

Substituting 15 into 14 we obtain

$$C_f = \frac{1}{\sqrt{Re}} \left(\left(1 + \frac{1}{\beta} \right) f''(0) + \frac{We}{2} f''^2(0) \right),$$

$$Sh = -\sqrt{Re} \phi(0),$$

$$Nu = -\sqrt{Re} \theta'(0).$$
(16)

where

$$Re = \frac{u_w x}{\nu}$$

is the Reynolds number.

2.2 Validation of the Flow Model

The validation of the model was carried out by comparing the present results for the Nusselt number represented by $(-\theta'(0))$ with the finding of [1] for different values of the Prandtl number (Pr) and for $A^* = B^* = M = K = Br = \beta = We = Nb = Ni = Sc = \omega = \lambda = 0$. The current results agree with their work. Table 1 illustrates the comparison.

Table 1: Computations indicating comparison with [1]

	[1]	Present Work
Pr	$-\theta'(0)$	$-\theta'(0)$
0.7	0.4539	0.4539
2.0	0.9113	0.9114
7.0	1.8954	1.8954

3 Results and Discussions

The coupled equations (9 – 11), along with the boundary conditions (12) and (13), are highly nonlinear and solved numerically using the fourth-order Range-Kutta method combined with the Newton-Raphson shooting technique. Numerical and graphical results are generated using Maple 20 software package. The thermophysical parameters incorporated into the analysis include the magnetic field parameter (M), velocity parameter (λ), permeability parameter (κ), chemical reaction parameter (ω), Prandtl number (Pr), thermophoresis parameter (N_t), Brownian motion parameter (N_b), Schmidt number (Sc), Brinkman nummber (B_r) and internal heat generation parameters (A_1) and (B_1). The study focuses on Williamson and Casson nanofluids. In the numerical and graphical representations, Williamson nanofluid is represented in black while Casson nanofluid is shown in blue.

Table 2: Computations showing $(-f''(0))$, $(-\theta'(0))$ and $(-\phi(0))$ for different parameter values.

Sc	N _b	N _t	ω	λ	A ₁	B ₁	M	K	Pr	Br	-f''(0)	-θ'(0)	-φ(0)
0.5	0.6	0.2	0.1	0.5	0.1	0.1	0.1	0.1	2	0.1	1.006773	0.504864	0.446874
											0.462431	0.537935	0.479269
											1.006773	0.374615	0.947017
											0.462431	0.400169	1.003715
											1.006773	0.382113	0.497919
											0.462431	0.408321	0.532711
											1.006773	0.278705	0.520217
											0.462431	0.239394	0.356026
											1.006773	0.496105	0.332347
											0.462431	0.528602	0.359535
											1.006773	0.489343	0.260457
											0.462431	0.521620	0.284235
											1.006773	0.459671	0.644514
											0.462431	0.495484	0.466991
											1.006773	0.429788	0.800366
											0.462431	0.466179	0.815143
											0.681135	0.537545	0.481761
											0.330274	0.558174	0.500409
											0.343913	0.566312	0.513859
											0.175414	0.576407	0.521894
											1.006773	0.252354	0.514318
											0.462431	0.274614	0.548739
											1.006773	0.004001	0.580412
											0.462431	0.015740	0.616834
											1.006773	0.375985	0.485243
											0.462431	0.421736	0.513716
											1.006773	0.228784	0.528663
											0.462431	0.292598	0.351784
											1.033336	0.506313	0.447449
											0.472391	0.539519	0.480494
											1.060417	0.507628	0.448024
											0.482414	0.541164	0.481725
											1.036011	0.502679	0.446356
											0.473225	0.555953	0.478652
											1.065042	0.500459	0.445869
											0.483888	0.534065	0.478068
											1.006773	0.669687	0.402152
											0.462431	0.703752	0.435052
											1.006773	0.805589	0.363553
											0.462431	0.837967	0.397546
											1.006773	0.327095	0.503228
											0.462431	0.258938	0.366879
											1.006773	0.130942	0.565368
											0.462431	0.047887	0.657786

Table 2 represents the influence of various thermophysical parameters on the skin friction coefficient $(-f''(0))$, Nusselt number $(-\theta'(0))$ and Sherwood number $(-\phi'(0))$ for both Williamson and Casson nanofluids. The skin friction coefficient quantifies the shear stress exerted by the fluid at the surface, the Nusselt number represents the ratio of convective to conductive heat transfer across a boundary while the Sherwood number expresses the ratio of convective mass transfer to the rate of diffusive mass transport. Table 2 shows that increasing the magnetic field parameter enhances the skin friction coefficient, Nusselt number and Sherwood number for both nanofluids, attributed to improved convective heat and mass transfer.

Williamson nanofluid demonstrated a higher skin friction coefficient while Casson nanofluid exhibited greater improvements in both Sherwood and Nusselt numbers. An increase in the the Schmidt number, Brownian motion parameter, thermophoresis parameter, chemical reaction parameter, Brinkman number and internal heat generation led to an increase in the Sherwood number but caused a reduction in the Nusselt number for both nanofluids as a result of enhanced conductive heat transfer. Casson nanofluid showed a higher Sherwood number while Williamson nanofluid provided better enhancement in the Nusselt number, indicating that Casson nanofluid is more suitable for applications requiring efficient species diffusion. The velocity ratio parameter was found to increase both the Nusselt and Sherwood numbers while reducing the skin friction coefficient for both nanofluids. Williamson nanofluid exhibited superior skin friction while Casson nanofluid yielded higher Nusselt and

Sherwood numbers. This behaviour is critical in optimizing processes such as extrusion and industrial cooling. An increase in the permeability parameter raised the skin friction coefficient but reduced both Nusselt and Sherwood numbers for both fluids, with Williamson nanofluid showing a higher skin friction coefficient and Casson nanofluid achieving greater Nusselt and Sherwood numbers. Additionally, a higher Prandtl number increased the Nusselt number but decreased the Sherwood number due to enhanced momentum diffusivity. Casson nanofluid exhibitd superior Nusselt number which makes it ideal for use in heat exchangers, thermal management systems and cooling devices. While Williamson nanofluid on the other hand enhanced the Sherwood number, which suggests its suitability for applications requiring efficient species diffusion, such as industrial mixing.

3.1 Graphical Results

3.1.1 Effects of Parameter Variation on Velocity Profiles

Figures 2 – 4 illustrate the effects of various thermophysical parameters on the velocity profiles of both Casson and Williamson nanofluids. Figure 2 shows the impact of magnetic field parameter on velocity profiles. It reveals that an increase in the magnetic field parameter enhances the velocity of both nanofluids. The velocity is more significant for Casson nanofluid, indicating greater sensitivity to magnetic effects compared to Williamson nanofluid. Figure 3 demonstrates the influence of the velocity ratio parameter, where an increase in this parameter leads to higher velocity profiles of both Casson and Williamson nanofluids. For Casson nanofluid, the increase is noticeable but slightly less than that in the Williamson nanofluid, indicating different responses to surface stretching, which turns to decrease the boundary layer thickness. Figure 4 illustrates the effect of the permeability parameter on the velocity profile. It is noted that an increase in the permeability parameter leads to a decrease in the velocity profiles of both nanofluids. This is because the porous medium provides resistance which increase the boundary layer thickness. For Casson nanofluid, the impact is less severe, showing that Casson fluid experiences less deceleration in a porous medium compared to Williamson nanofluid. Casson nanofluid exhibits greater sensitivity magnetic fields and maintain higher velocity in porous media while Williamson nanofluid was noted to respond more significantly to changes in surface stretching. For applications involving strong magnetic fields or porous media, Casson nanofluid will be more advantageous, While for scenarios where surface stretching is predominant, Williamson nanofluid could be preferable.

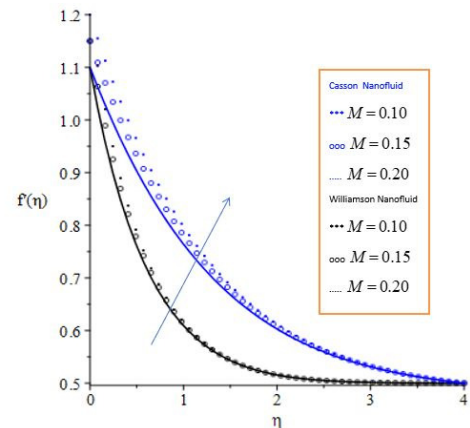


Fig. 2: Velocity Profile for varying values of the magnetic field parameter for $Br = 0.1, Sc = 0.5, \beta = 0.4, We = 0.4, A_1 = 0.1, B_1 = 0.1, \omega = 0.1, Pr = 2, N_t = 0.1, N_b = 0.5, \lambda = 0.5,$ and $K = 0.1$

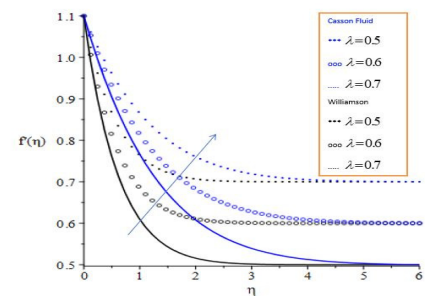


Fig. 3: Velocity Profile for varying values of velocity ratio parameter for $Br = 0.1, Sc = 0.5, \beta = 0.4, We = 0.4, A_1 = 0.1, B_1 = 0.1, \omega = 0.1, Pr = 2, N_t = 0.1, N_b = 0.5, M = 0.1,$ and $K = 0.1$

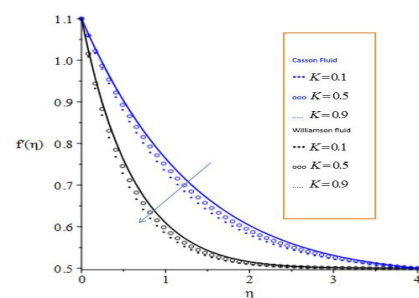


Fig. 4: Velocity profile for varying values of the porosity parameter with $Br = 0.1, Sc = 0.5, \beta = 0.4, We = 0.4, A_1 = 0.1, B_1 = 0.1, \omega = 0.1, Pr = 2, N_t = 0.1, N_b = 0.5, M = 0.1,$ and $\lambda = 0.5.$

3.1.2 Effects of Parameter Variation on Temperature Profile

Figure 5 – 9 demonstrate the influence of various thermo-physical parameters on the temperature profiles of both Casson and Williamson nanofluids. In figure 5, it is observed that an increase in Brownian motion parameter raises the temperature profile for both nanofluids, as enhanced thermal conductivity results from the motion of nanoparticles. Similarly, figures 6 and 7 show that an increase in internal heat generation raises the temperature profile of both nanofluids, as additional internal heat source contributes to the thermal energy within the fluids, elevating the overall temperature. In Figure 8, higher values of the thermophoresis parameter are found to increase the temperature profile of both nanofluids, as thermophoresis causes particles to migrate from hot to cold regions, which intensifies the temperature gradient and increases the temperature distribution. Figure 9 illustrates that an increase in the Brinkman number results in a higher temperature profile of both fluids due to the heat generated by viscous dissipation. Finally, in figure 10, an increase in the Prandtl number leads to a decrease in the temperature profile of both nanofluids. This occurs because nanofluids with a higher prandtl number experiences more confined thermal diffusivity near the boundary, reducing the temperature profile across the nanofluids. Both Casson and Williamson nanofluid show an increment in temperature profile with Brownian motion and thermophoresis parameters. Also, while both nanofluids respond to internal heat generation and viscous dissipation, their specific heat capacities and thermal conductivity ratios affected the degree of temperature increase.

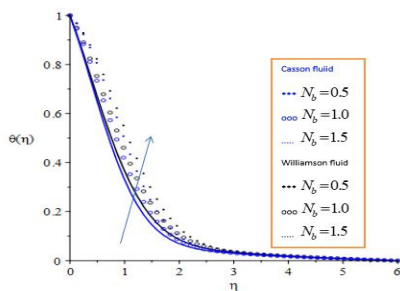


Fig. 5: Temperature Profile for varying values of Brownian motion parameter for $Br = 0.1, Sc = 0.5, \beta = 0.4, We = 0.4, A_1 = 0.1, B_1 = 0.1, \omega = 0.1, Pr = 2, N_t = 0.1, K = 0.1, M = 0.1,$ and $\lambda = 0.5$

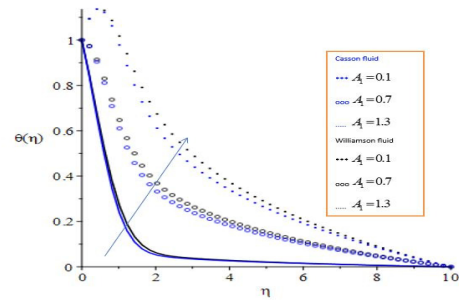


Fig. 6: Temperature Profile for varying values of internal heat generation parameter for $Br = 0.1, Sc = 0.5, \beta = 0.4, We = 0.4, N_b = 0.5, B_1 = 0.1, \omega = 0.1, Pr = 2, N_t = 0.1, K = 0.1, M = 0.1,$ and $\lambda = 0.5$

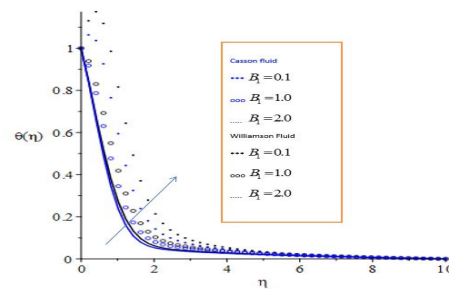


Fig. 7: Temperature Profile for varying values of internal heat generation parameter for $Br = 0.1, Sc = 0.5, \beta = 0.4, We = 0.4, N_b = 0.5, A_1 = 0.1, \omega = 0.1, Pr = 2, N_t = 0.1, K = 0.1, M = 0.1,$ and $\lambda = 0.5$

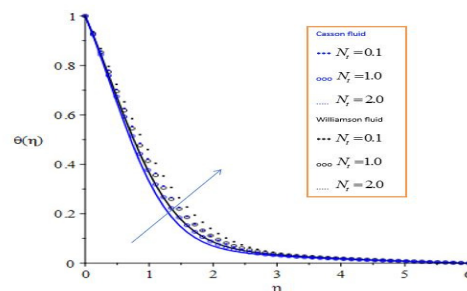


Fig. 8: Temperature Profile for varying values of thermophoresis parameter for $Br = 0.1, Sc = 0.5, \beta = 0.4, We = 0.4, N_b = 0.5, A_1 = 0.1, \omega = 0.1, Pr = 2, B_1 = 0.1, K = 0.1, M = 0.1,$ and $\lambda = 0.5$

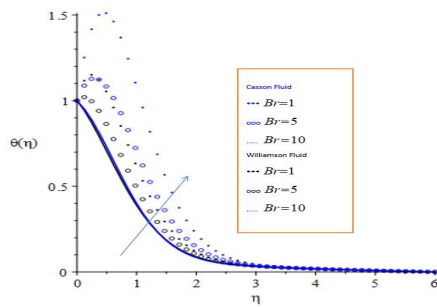


Fig. 9: Temperature Profile for varying values of Brinkmann number for $N_t = 0.1$, $Sc = 0.5$, $\beta = 0.4$, $We = 0.4$, $N_b = 0.5$, $A_1 = 0.1$, $\omega = 0.1$, $Pr = 2$, $B_1 = 0.1$, $K = 0.1$, $M = 0.1$, and $\lambda = 0.5$

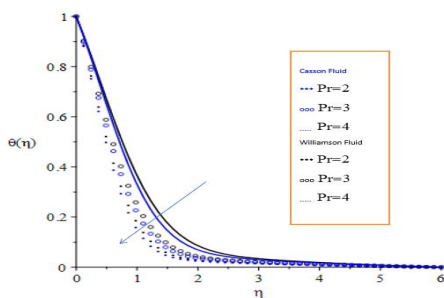


Fig. 10: Temperature Profile for varying values of Prandtl number for $N_t = 0.1$, $Sc = 0.5$, $\beta = 0.4$, $We = 0.4$, $N_b = 0.5$, $A_1 = 0.1$, $\omega = 0.1$, $Br = 0.1$, $B_1 = 0.1$, $K = 0.1$, $M = 0.1$, and $\lambda = 0.5$

3.1.3 Effects of Parameter Variation on Concentration Profile

Figure 11 – 18 show the effects of various thermo-physical parameters on the concentration profile of both Casson and Williamson nanofluids. In figure 11, the impact of the thermophoresis parameter on the concentration profile is illustrated. It is observed that an increase in this parameter enhances the concentration profile of both nanofluids. This occurs because thermophoresis causes particles to migrate from hotter to cooler regions, increasing the concentration. In figure 12, the effects of Brownian motion parameter on the concentration profile are shown. It is found that increasing the Brownian motion parameter leads to a lower concentration profile of both nanofluids due to the random movement of nanoparticles that promotes better mixing and distribution. Figure 13 illustrates the effects of the velocity ratio parameter on the concentration profile. It is observed that an increase in the velocity ratio parameter reduces the concentration profile of both

nanofluids, as convection effects dominate over diffusion. Figure 14 shows that the concentration profile decrease as the Brinkman number increases for both nanofluids due to enhanced dispersion effects from viscous heating. In figure 15, the effects of the Schmidt number on the concentration profile are demonstrated. It is observed that an increase in the Schmidt number decreases the concentration profile, as higher Schmidt numbers indicate lower mass diffusivity, which reduces the concentration of both nanofluids. Figure 16 shows that an increase in the chemical reaction parameter decreases the concentration profile of both nanofluids, as higher reaction rates consume reactant more quickly, lowering the concentration of nanoparticles in the fluids. Finally, figures 17 and 18 show that an increase in the internal heat generation parameter reduces the concentration profile. This is due to the additional heat within the nanofluids, which promotes better nanoparticle dispersion due to increased thermal motion.

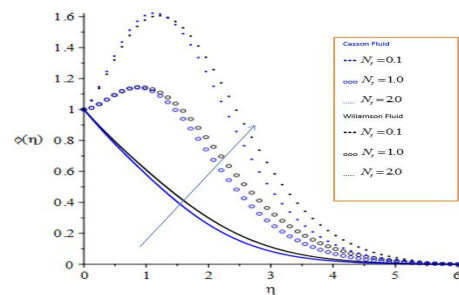


Fig. 11: Concentration Profile for varying values of the thermophoresis parameter for $Pr = 2$, $Sc = 0.5$, $\beta = 0.4$, $We = 0.4$, $N_b = 0.5$, $A_1 = 0.1$, $\omega = 0.1$, $Br = 0.1$, $B_1 = 0.1$, $K = 0.1$, $M = 0.1$, and $\lambda = 0.5$

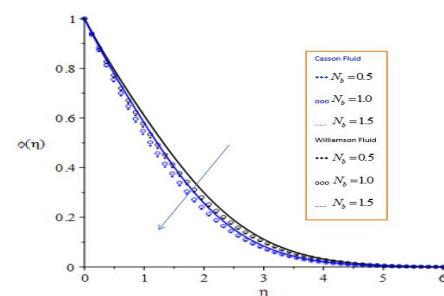


Fig. 12: Concentration Profile for varying values of the Brownian motion parameter for $Pr = 2$, $Sc = 0.5$, $\beta = 0.4$, $We = 0.4$, $N_t = 0.1$, $A_1 = 0.1$, $\omega = 0.1$, $Br = 0.1$, $B_1 = 0.1$, $K = 0.1$, $M = 0.1$, and $\lambda = 0.5$

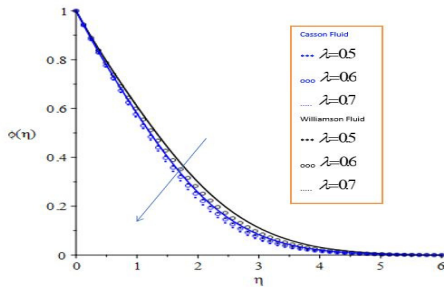


Fig. 13: Concentration Profile for varying values of velocity ratio parameter for $Pr = 2$, $Sc = 0.5$, $\beta = 0.4$, $We = 0.4$, $N_t = 0.1$, $A_1 = 0.1$, $\omega = 0.1$, $Br = 0.1$, $B_1 = 0.1$, $K = 0.1$, $M = 0.1$, and $N_b = 0.5$

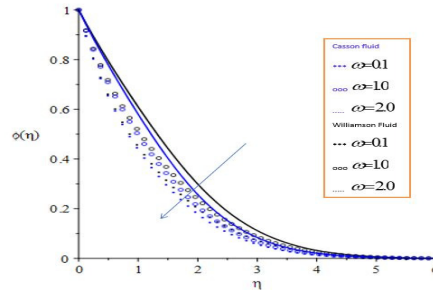


Fig. 16: Concentration Profile for varying values of rate of chemical reaction

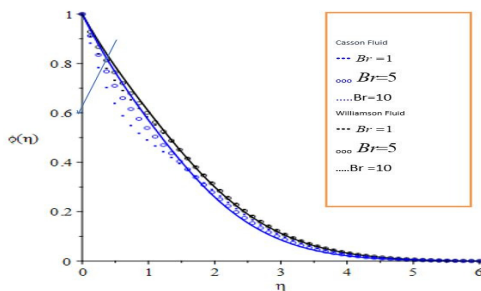


Fig. 14: Concentration for varying values of Brinkmann number for $Pr = 2$, $Sc = 0.5$, $\beta = 0.4$, $We = 0.4$, $N_t = 0.1$, $A_1 = 0.1$, $\omega = 0.1$, $\lambda = 0.5$, $B_1 = 0.1$, $K = 0.1$, $M = 0.1$, and $N_b = 0.5$

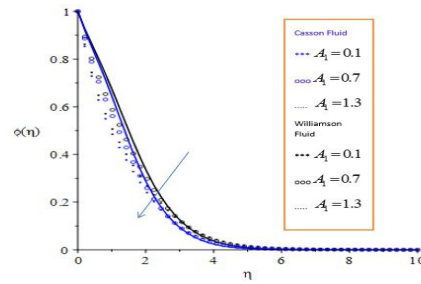


Fig. 17: Concentration Profile for varying values of Internal heat generation parameter for $Pr = 2$, $Br = 0.1$, $\beta = 0.4$, $We = 0.4$, $N_t = 0.1$, $\omega = 0.1$, $SC = 0.5$, $\lambda = 0.5$, $B_1 = 0.1$, $K = 0.1$, $M = 0.1$, and $N_b = 0.5$

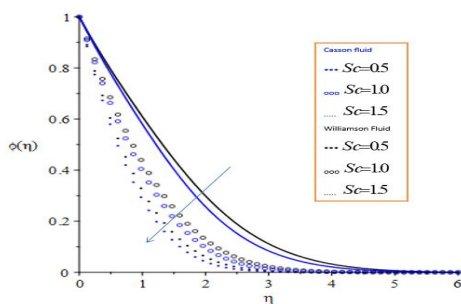


Fig. 15: Concentration Profile for varying values of Schmidt number for $Pr = 2$, $Br = 0.1$, $\beta = 0.4$, $We = 0.4$, $N_t = 0.1$, $A_1 = 0.1$, $\omega = 0.1$, $\lambda = 0.5$, $B_1 = 0.1$, $K = 0.1$, $M = 0.1$, and $N_b = 0.5$

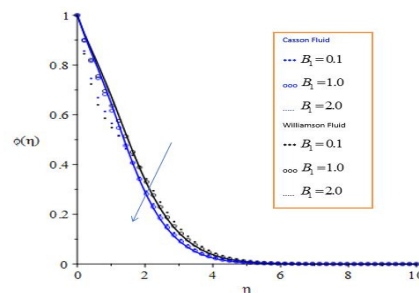


Fig. 18: Concentration Profile for varying values of Internal heat generation parameter for $Pr = 2$, $Br = 0.1$, $\beta = 0.4$, $We = 0.4$, $N_t = 0.1$, $A_1 = 0.1$, $SC = 0.5$, $\lambda = 0.5$, $\omega = 0.1$, $K = 0.1$, $M = 0.1$, and $N_b = 0.5$

4 Conclusion

The effects of non-uniform heat generation on boundary layer flow of magnetized Casson-Williamson nanofluid

towards a dissipative stagnation point have been investigated. Similarity variables were used to transform the governing partial differential equations into a system of coupled nonlinear differential equations. Numerical solutions to these equations were obtained using the fourth-order Runge-Kutta method combined with the Newton-Raphson shooting technique. The study leads to the following general conclusions:

- i. Williamson nanofluid is observed to have a higher skin friction coefficient than Casson nanofluid across all embedded thermo-physical parameter, making it a suitable choice for enhancing the performance of brake fluid.
- ii. Casson nanofluid exhibits a higher mass transfer rate but a lower heat transfer rate, whereas Williamson nanofluid shows the opposite trend under the influence of Brownian motion, thermophoresis and internal heat generation parameters.
- iii. The magnetic field and velocity ratio parameters are found to significantly enhance the fluid velocity within the momentum boundary layer of Casson nanofluid than that of Williamson nanofluid.
- iv. Internal heat generation and Brownian motion parameters are observed to significantly increase the temperature of the fluid within the thermal boundary layer of Williamson nanofluid compared to Casson nanofluid.
- v. The thermophoresis parameter is observed to greatly enhance the concentration of the fluid within the Solutal boundary layer of Williamson nanofluid compared to Casson nanofluid.

Acknowledgement The authors are grateful to the anonymous referees for a careful checking of the details and for helpful comments that improved this paper.

References

- [1] R.S. Gorla and I. Sidawi, *Applied Scientific Research* **52**, 247–257 (1994).
- [2] A. Ishak, R. Nazar, and I. Pop, Mixed convection boundary layers in the stagnation-point flow toward a stretching vertical sheet, *Meccanica* **41**, 509–518 (2006).
- [3] S. Nadeem, A. Hussain, and M. Khan, HAM solutions for boundary layer flow in the region of the stagnation point towards a stretching sheet, *Commun. Nonlinear Sci. Numer. Simul.* **15**(3), 475–481 (2010).
- [4] K. Bhattacharyya, Effects of radiation and heat source/sink on unsteady MHD boundary layer flow and heat transfer over a shrinking sheet with suction/injection, *Front. Chem. Sci. Eng.* **5**(3), 376–384 (2011).
- [5] S. Mukhopadhyay, Casson fluid flow and heat transfer over a nonlinearly stretching surface, *Chin. Phys. B* **22**(7), 074–701 (2013).
- [6] F. Mabood, W.A. Khan, and A.M. Ismail, MHD boundary layer flow and heat transfer of nanofluids over a nonlinear stretching sheet: a numerical study, *J. Magn. Magn. Mater.* **374**, 569–576 (2015).
- [7] I.Y. Seini, G. Aloliga, B. Ziblim, and O.D. Makinde, Boundary layer flow of Casson fluid on exponentially stretching porous surface with radiative heat transfer, *Diffus. Found.* **26**, 112–125 (2020).
- [8] G. Aloliga, I.Y. Seini, and R. Musah, Heat transfer in a magnetohydrodynamic boundary layer flow of a non-Newtonian Casson fluid over an exponentially stretching magnetized surface, *J. Nanofluids* **10**(2), 172–185 (2021).
- [9] P.P. Humane, V.S. Patil, and A.B. Patil, Chemical reaction and thermal radiation effects on magnetohydrodynamics flow of Casson-Williamson nanofluid over a porous stretching surface, *Proc. Inst. Mech. Eng. Part E: J. Process Mech. Eng.* **235**(6), 2008–2018 (2021).
- [10] H. Alrihieli, M. Areshi, E. Alali, and A.M. Megahed, MHD dissipative Williamson nanofluid flow with chemical reaction due to a slippery elastic sheet in a porous medium, *Micromachines* **13**(11), 1879 (2022).
- [11] R.P. Sharma and S. Shaw, MHD non-Newtonian fluid flow past a stretching sheet under the influence of non-linear radiation and viscous dissipation, *J. Appl. Comput. Mech.* **8**(3), 949–961 (2022).
- [12] A.M. Alqahtani, M. Bilal, M. Usman, T.R. Alsenani, A. Ali, and S.R. Mahmood, Heat and mass transfer through MHD Darcy Forchheimer Casson hybrid nanofluid flow across an exponential stretching sheet, unpublished manuscript.
- [13] T. Gladys and G.V. Reddy, Soret-Dufour mechanisms on thermal loading of Cattaneo-Christov theories on MHD Casson nanofluid dynamics over a stretching sheet, *J. Nanofluids* **12**(6), 1475–1484 (2023).
- [14] H. Muzara and S. Shateyi, Magnetohydrodynamics Williamson nanofluid flow over an exponentially stretching surface with a chemical reaction and thermal radiation, *Mathematics* **11**(12), 2740 (2023).
- [15] Y.O. Tijani, M.T. Akolade, H.A. Ogunseye, A.T. Adeosun, and O. Farotimi, On generalized Fick's and Fourier's laws for unsteady Casson-Williamson fluids over a stretching surface: A spectral approach, *J. Nanofluids* **12**(1), 91–103 (2023).
- [16] M.Z. Ahmed, V. Dhanalaxmi, and S. Panda, Thermal analysis on Ferro Casson nanofluid flow over a Riga plate with thermal radiation and non-uniform heat source/sink, *Mod. Phys. Lett. B* **2450460** (2024).
- [17] G.S. Mini, P.V. Kumar, and M.I. Shaik, Numerical simulations of chemically dissipative MHD mixed convective non-Newtonian nanofluid stagnation point flow over an inclined stretching sheet with thermal radiation effects, *CFD Lett.* **16**(5), 37–58 (2024).



Mathias John Fuseini is a masters student in mathematics at C. K. Tedom University of Technology and Applied Sciences, Ghana.



Christian John Etwire is a senior lecturer and the Head of Department of Mathematics at C. K. Tedom University of Technology and Applied Sciences, Ghana. He received his PhD degree in Mathematics from the University for Development Studies, Ghana. His research interests include: computational fluid

dynamics, mathematical modelling and optimization. He has published several research articles in reputable mathematical and engineering journals.